

Kramers-Weyl fermions

Guoqing Chang^{*,1,2} Daniel S. Sanchez^{*,3} Benjamin J. Wieder^{*,4} Su-Yang Xu^{*,3}
 Frank Schindler^{*,5} Ilya Belopolski^{,3} Shin-Ming Huang,⁶ Bahadur Singh,^{1,2} Di
 Wu,^{1,2} Titus Neupert,⁷ Tay-Rong Chang,⁸ Hsin Lin,^{1,2,†} and M. Zahid Hasan^{3,9,‡}

¹*Centre for Advanced 2D Materials and Graphene Research Centre,
 National University of Singapore, 6 Science Drive 2, 117546, Singapore*

²*Department of Physics, National University of Singapore,
 2 Science Drive 3, 117546, Singapore*

³*Laboratory for Topological Quantum Matter and Spectroscopy (B7),
 Department of Physics, Princeton University,
 Princeton, New Jersey 08544, USA*

⁴*Department of Physics and Astronomy,
 University of Pennsylvania, Philadelphia, Pennsylvania 19104, USA*

⁵*Department of Physics, University of Zurich,
 Winterthurerstrasse 190, 8057 Zurich, Switzerland*

⁶*Department of Physics, National Sun Yat-Sen University, Kaohiung 804, Taiwan*

⁷*Department of Physics, University of Zurich,
 Winterthurerstrasse 190, 8057 Zurich, Switzerland*

⁸*Department of Physics, National Tsing Hua University, Hsinchu 30013, Taiwan*

⁹*Princeton Institute for Science and Technology of Materials,
 Princeton University, Princeton, New Jersey, 08544, USA*

(Dated: November 24, 2016)

* These authors contributed equally to this work.

Abstract

Symmetry places strong constraints on the electronic features of crystals. By considering the role of time-reversal, \mathcal{T} , symmetry in structurally chiral crystals with significant spin-orbit interaction, we show that Kramers theorem may lead to the realization of topologically robust Weyl fermionic excitations *pinned* to the time-reversal-invariant crystal momenta. By constructing a tight-binding model for \mathcal{T} -invariant chiral crystals in space group 16 (SG-16), we demonstrate the conditions under which Kramers theorem-enforced Weyl fermions are universal features. We identify their unique topological properties and use density functional theory to predict that Ag_3BO_3 (SG-156), TlTe_2O_6 (SG-150), and Ag_2Se (SG-19) are examples of Kramers theorem-enforced Weyl metals. Our results demonstrate a methodology that can be utilized for identifying novel gapless topological states in real materials.

Time-reversal symmetry is one of the most fundamental symmetries of nature. Classically, it is associated with the perfect reversibility of an individual particle's path. In quantum mechanics, it is represented by invariance under an anti-unitary operator \mathcal{T} . For the electrons in a crystal, \mathcal{T} flips the crystal momentum $\mathbf{k} \rightarrow -\mathbf{k}$, such that Time-Reversal-Invariant crystal Momenta (TRIMs) occur typically at values $k = 0, \pi$. When acting on spinful particles, \mathcal{T} -symmetry has the further effect of flipping the spin, which has a fundamental consequence when time-reversal is imposed twice. For particles with integer spin (bosons), \mathcal{T}^2 is equivalent to an identity operation, whereas for particles of half-integer spin (fermions) a factor of -1 is acquired. This minus sign also implies Kramers theorem: every state has at least one degenerate partner. Thus, in a \mathcal{T} -symmetric crystal of fermionic particles, while the band degeneracy generically unrestricted at most crystal momenta, twofold Kramers degeneracies at the TRIMs *will always be present*.

Chirality, or in three-dimensions a sense of handedness, is a fundamental geometric feature in nature. It is permitted under the breaking of all roto-inversion symmetries, or the combined operations of spatial inversion and uniaxial rotation. Chiral objects therefore share the geometric property of being non-superimposable by a pure rotation and translation onto their images under spatial inversion. Though most commonly applied to discussions of human hands and DNA helices, chirality can also sometimes characterize the arrangement of atoms in a crystal. Specifically, a chiral (Sohncke) crystal is left invariant under symmetry operations of the first kind only (rotations and translations) and none of the second kind (inversion through a point, reflection through a plane, and other roto-inversions) [1].

In this paper, we find that in \mathcal{T} -symmetric chiral crystals, Kramers theorem may enforce the presence of topologically nontrivial Weyl fermions at TRIMs, resulting in a previously uncharacterized topological Weyl metal phase. We classify the topological nodal physics that is guaranteed in symmorphic chiral space groups and possible in non-symmorphic chiral space groups due to Kramers theorem. Specifically, we show that for *all* symmorphic chiral space groups *all* Kramers-theorem-enforced twofold degeneracies at the TRIM are Weyl fermionic excitations that can not be pairwise annihilated. For non-symmorphic chiral space groups, we find that the specific details of the symmetry group determine whether or not Weyl nodes will be found at the TRIMs. In order to investigate the topological features present in symmorphic chiral space groups, we construct a tight-binding model in space group 16 (SG-16) and identify material candidates that realize these novel Kramers theorem-enforced

Weyl fermions. We identify the distinct features of Kramers Weyl metals and show that they differ significantly from familiar band-inversion-generated Weyl semimetals. Though early research has touched indirectly on possible relationships between time-reversal-symmetry and Weyl fermion physics [2, 3], we present for the first time a fundamental relationship between these two phenomena. In addition, our results provide a novel and practical recipe that facilitates the search for new topological Weyl phases in real crystals.

I. Band-inversion generated Weyl nodes

In relativistic quantum mechanics, Weyl fermions are described by a two-component chiral spinor, and represent in some sense “half” of a massless Dirac fermion. [4]. Although Weyl fermions have yet to be experimentally verified in the realm of high-energy physics, they have recently been realized as twofold-degenerate fermionic excitations in single crystals and in three-dimensional optical lattices [5–11]. In these previous realizations, Weyl nodes manifest pairwise at generic \mathbf{k} points through a band-inversion process [12–33]. Although these band-inversion topological Weyl semimetals are robust against all perturbations that preserve translation invariance, they may be pushed to a gapped phase by pairwise annihilation of Weyl nodes of opposite chiral charge [12–15], *while preserving all symmetries of the system*. The novel Kramers Weyl metals presented in this work do not share this property.

In Fig. 1, we compare the two topological Weyl phases and highlight the uniqueness of a Kramers theorem-enforced Weyl metal. Displayed in Fig. 1a, the Weyl nodes of a \mathcal{T} -invariant, inversion (\mathcal{I}) symmetry breaking, band-inversion Weyl semimetal are shown to manifest pairwise at generic points on the (k_1, k_2) -surface, with blue and red coloring indicating opposite chiral charge. The extent of such a band-inversion may be reduced, and even completely removed, by tuning crystal parameters such as spin-orbit coupling (SOC) and lattice spacing. As the band-inversion is reduced, the Weyl nodes may approach each other and eventually pairwise annihilate to open a band gap, as displayed in the rightmost panel in Fig. 1a. Similarly, a band-inversion can also pairwise create Weyl nodes in \mathcal{I} -invariant, \mathcal{T} -breaking, Weyl semimetals [16]. In fact, all Weyl semimetals candidates predicted until now, whether \mathcal{I} - or \mathcal{T} -breaking, type-I or type-II, spinless or spinful, have required a band-inversion operation [12–33]. The question therefore arises whether a band-inversion operation is always necessary for creating Weyl nodes. We find that the answer is an emphatic no.

II. Kramers theorem-enforced Weyl nodes

To illustrate the unique features of Kramers Weyl nodes and contrast them with band-inversion Weyl nodes, we provide in Fig. 1b an example of the electronic band structure of a generic chiral crystal. The chiral charge distribution at all TRIMs on the (k_1, k_2) surface is shown in the leftmost panel in Fig. 1b. An energy-dispersion cut along the Kramers Weyl nodes shows that each TRIM hosts an isolated twofold-degenerate linearly-dispersing node, as shown in the middle panel Fig. 1b. One novel aspect of the Kramers Weyl nodes is their behavior as the strength of SOC is increased. In the rightmost panel of Fig. 1b, we show that when SOC is much stronger than lattice hopping, the singly-degenerate bands become further separated while the Kramers Weyl nodes remain pinned at the TRIMs. Furthermore, as shown in the following sections, since Kramers Weyl nodes have their oppositely chiral charged partners at neighboring TRIMs, they provide an example of the *largest possible* Weyl node separation in momentum space.

As a result of their reliance on \mathcal{T} -symmetry and lattice chirality, Kramers Weyl nodes *may not be annihilated without altering the collection of system symmetries*, unlike band-inversion generated Weyl nodes. One such route involves breaking \mathcal{T} -symmetry and highly distorting the bands such that the Weyl nodes are dislodged from the TRIMs. The only other possible route towards nullifying the topological physics in Kramers Weyl metals is to induce a structural transition that changes the system space group and introduces a roto-inversion symmetry, such as mirror symmetry. We illustrate in Fig. 1c that this addition of extra symmetries gives rise to extra band degeneracies that connect neighboring Kramers points along particular k -space directions. In this figure, we show the distribution of trivial Kramers points on the TRIMs for the (k_1, k_2) surface in the leftmost panel, which are displayed as black marks to convey their lack of chiral charge. As is shown in the middle and rightmost panel in Fig. 1c, under the presence of an additional roto-inversion symmetry, it is no longer true that the Kramers points are entirely isolated, and therefore they can no longer carry a well-defined topological index.

III. Tight-binding model for symmorphic chiral SG-16:

To better understand how topologically non-trivial Kramers points must arise in symmorphic chiral crystal structures, we present a simple tight-binding model in space group 16 (SG-16) ($P222$). Though this model is specific to SG-16, conclusions drawn from it

generically apply to the relevant Weyl physics in all 26 symmorphic chiral space groups as well. Space group 16 is defined by a noncentrosymmetric orthorhombic crystal structure with twofold rotations along each principle axis x, y, z . We consider a 1-site unit cell on a primitive orthorhombic lattice with a spin-1/2 degree of freedom on each site. Considering all symmetry-allowed nearest neighbor hopping terms, the tight-binding Hamiltonian reads

$$\mathcal{H}(\mathbf{k}) = \sum_{i=x,y,z} t_i^1 \cos(k_i) + t_i^s \sin(k_i) \sigma^i \quad (1)$$

with $t_i^1 \neq t_j^1 \neq t_i^s \neq t_j^s \forall i \neq j$. Here t_i^1 denotes the s-orbital-like hopping strength and t_i^s is a spin-orbit term. By examining each TRIM at the $\mathbf{k} \cdot \mathbf{p}$ level, we observe that each point is a Weyl node described by

$$\mathcal{H}_{\mathbf{k} \cdot \mathbf{p}} = \sum_{i=x,y,z} \left[u_i \left(1 - \frac{k_i^2}{2} \right) + v_i k_i \sigma^i \right], \quad (2)$$

where in our model each TRIM has the same magnitude of u_i and v_i inherited from the lattice hopping parameters, but differing TRIM-specific signs. The wavefunction for the lower band is $|u^- \rangle$ for an arbitrary spin-1/2 system with a linear relationship between the trigonometric functions of the angles and \mathbf{k} . Hence, when integrated around a sphere \mathcal{S} enclosing the Weyl node, the Berry curvature \mathcal{F} of the lower band also wraps around the surface of a sphere exactly once. Therefore, the magnitude of the Chern numbers $C = \frac{1}{2\pi} \int \mathcal{F} d\mathcal{S}$ of the Kramers Weyl nodes is $|C| = 1$ at all TRIMs. In Figs. 2b,c, we show the resulting band structure for this SG-16 tight-binding model in the absence and presence of SOC interactions, respectively. As expected, the inclusion of SOC splits the twofold degenerate band in Fig. 2b and generates isolated twofold-degenerate Kramers-theorem-enforced nodes at all of the TRIMs (Fig. 2c) [34, 35]. To determine the chiral charge of each Kramers Weyl node, we examine the direction of the wrapping of \mathcal{F} given by the relative signs of the $\{v_i\}$ (the overall sign exchanges $|u^\pm \rangle$) to find the Chern number

$$C = \prod_{i=x,y,z} \text{sgn}(v_i), \quad (3)$$

where $|u^\pm \rangle$ is the wavefunction for the upper and lower bands. This result indicates that the chiral charge $C_{+1} = +1 \times \text{sgn}(t_x^s t_y^s t_z^s)$ for the Kramers pairs at TRIM points Γ , S , U , and T and $C_{-1} = -1 \times \text{sgn}(t_x^s t_y^s t_z^s)$ for the pairs at X , Y , Z , and R , as illustrated in Fig. 2a. Consistent with the Nielsen-Ninomiya theorem requiring conservation of chiral

charge [36], we observe that there is an equal number of +1 and -1 chiral charges in the system. Furthermore, the sign of C at Γ reflects the signs of the $\{t_i^s\}$ for the position space lattice. Thus, the chirality of the atomic positions is directly responsible for defining the handedness of the Kramers Weyl node at Γ and therefore, by the pattern of alternating signs, at all of the other TRIMs as well.

We note that whereas all TRIMs in SG-16 will display Kramers Weyl nodes with Chern number $|C| = 1$, this need not be the case if higher-order rotational symmetries are present. In the supplemental material, we demonstrate that in chiral crystals with \mathcal{C}_6 rotational symmetries, Kramers Weyl nodes with Chern number $|C| = 3$ can be enforced. Furthermore, we show that in general, spinful time-reversal symmetry restricts Kramers-Weyl nodes (as degeneracies between two bands) to have odd Chern numbers.

As chirality can be nullified by introducing a roto-inversion symmetry operation $\mathcal{S}_{nv} = \mathcal{I}\mathcal{C}_{nv}$, where \mathcal{C}_{nv} is an n -fold rotation along \mathbf{v} , we analyze the result of adding mirror symmetries $\mathcal{M}_v = \mathcal{I}\mathcal{C}_{2v}$. At the $\mathbf{k} \cdot \mathbf{p}$ level, we observed that $\mathcal{M}_i = i\sigma^i \otimes (k_i \rightarrow -k_i)$ has the same form at all eight TRIMs and, consequently, destroys the Kramers Weyl nodes by disallowing linear dispersion in at least one direction. A similar effect occurs when inversion symmetry \mathcal{I} is added to our tight-binding model; all bands become twofold degenerate. In practice, this implies the possibility of eliminating the topological character of Kramers Weyl nodes by a structural transition to a configuration with higher symmetry.

We note that it *is* possible for a noncentrosymmetric, achiral crystal to host a Kramers Weyl nodes if not all of its TRIMs lie in its mirror planes. We discuss this in further detail in the supplemental material.

Equation (2) is, to second order in \mathbf{k} , the most general $\mathbf{k} \cdot \mathbf{p}$ Hamiltonian of any Kramers degeneracy at *any* TRIM in SG-16. Note that whereas the nodes in a band-inversion Weyl semimetal can be tilted by a scalar term into Type-II Weyl nodes [24], Kramers Weyl nodes are prevented from this tilting by time-reversal symmetry.

The velocity terms in Eq. (2) take the form of a Dresselhaus spin-orbit coupling term $\mathbf{k} \cdot \boldsymbol{\sigma}$. Therefore, unlike for Weyl nodes in a band-inversion Weyl semimetal, the σ^i here act directly on the electron spin, rather than on some spin-orbit-coupled effective degree of freedom. Consequently, the eigenstates of Hamiltonian (2) obey strict spin-momentum locking, such that a Fermi surface enclosing the Kramers Weyl node will display the spin structure of a hedgehog topological defect. These hedgehog Berry curvature monopoles

could be probed directly by spin-resolved bulk angle photoemission.

Nonsymmorphic chiral SG-19:

It is important to clarify our specialization to symmorphic chiral crystals. A nonsymmorphic symmetry, i.e., a symmetry composed of the operation of a mirror or rotation followed by a fractional lattice translation, can lead to additional band degeneracies at the BZ edge and eliminate some of the topological physics in Kramers Weyl metals. Consider, for example, the chiral space group SG-19 ($P2_12_12_1$), which differs from SG-16 in that all of its twofold rotations are instead nonsymmorphic screws: $s_x = \{C_{2x}|\frac{1}{2}\frac{1}{2}0\}$, $s_y = \{C_{2y}|0\frac{1}{2}\frac{1}{2}\}$, and $s_z = \{C_{2z}|\frac{1}{2}0\frac{1}{2}\}$. In reciprocal space, $s_i \times \mathcal{T}$ are valid symmetry operations that map a \mathbf{k} point to itself on the $k_i = 0, \pi$ planes. When acting on a Bloch eigenstate of the Hamiltonian, $(s_i \mathcal{T})^2 = e^{-ik_i}$, and therefore enforces twofold Kramers degeneracies throughout all three $k_i = \pi$ planes (TRIMs belonging to multiple nodal planes will host fourfold degeneracies, i.e., 3D Dirac fermions, due to the algebra of the screw rotations at those \mathbf{k} points. [35, 37, 38]). These nodal planes may cover the surface projections of Kramers Weyl nodes elsewhere in the BZ, and therefore Fermi arcs may not be observable. Therefore generically, nonsymmorphic chiral crystals are not ideal candidates for observing topological Weyl *surface* physics.

However, some of the *bulk* physical properties of Kramers Weyl metals can survive the presence of nonsymmorphic symmetries. In SG-19, the Γ point, which belongs to none of the nodal planes, still features Kramers Weyl nodes with the same effective $\mathbf{k} \cdot \mathbf{p}$ Hamiltonian (2) as the Kramers Weyl nodes in symmorphic SG-16. More generally, though symmorphic chiral groups are guaranteed to have isolated Kramers Weyl nodes at every TRIM, *all* 65 chiral (Sohncke) space groups will still have Kramers Weyl nodes fixed at Γ . As all of the bulk probes of topologically nontrivial Fermi surfaces still apply to Kramers Weyl metals, as long as there are isolated Weyl nodes, there is hope for a nontrivial measurement. Therefore, nonsymmorphic chiral crystals, while hosting a more complicated topological band character than their symmorphic counterparts, could still possibly display topologically nontrivial bulk transport signatures. In the materials section, we present β -Ag₂Se (SG-19) as a candidate system for Kramers Weyl physics.

IV. Bulk analysis of symmorphic chiral SG-16 tight-binding model:

The bulk topological properties associated with Kramers Weyl nodes in symmorphic chiral

crystals are also distinct. Using our SG-16 tight-binding model, we examine the bulk Fermi surfaces at energy levels E_1 , E_2 , and E_3 (annotated in Fig. 2c) in Figs. 2d-f, respectively. The red and blue Fermi surfaces carry Chern number +1 and -1, respectively. At energy level E_1 , we observe two concentric spheres enclosing the R -points. As the energy level is increased from E_2 to E_3 , the red Fermi surface carrying a +1 Chern number splits into two, as shown in Fig. 2f. Interestingly, unlike in previously studied band-inversion Weyl semimetals [12–33], which only have non-trivial Fermi surfaces in the vicinity of the Weyl nodes, Kramers Weyl metals host topologically non-trivial Fermi surfaces over a drastically wider energy range.

V. Fermi surface analysis of symmorphic chiral SG-16 tight-binding model:

Comparing the Fermi surface evolution of Kramers Weyl metals to band-inversion Weyl semimetals, there is a notable contrast in topological character. Consider the electronic band structure of a band-inversion Weyl semimetal, shown in Fig. 3a, in which the energy levels of interest for Fermi surface analysis are labeled as E_1 , E_2 , and E_3 and the critical points that correspond to Lifshitz transitions are marked in yellow. Starting at an energy level that is well above the band-inversion Weyl nodes, E_3 , we observe that the bulk Fermi surface (whose boundary is defined by the black closed contour) encloses the projection of both oppositely chiral charged Weyl nodes and is, therefore, topologically trivial, as shown in the leftmost panel of Fig. 3b. Lowering the energy level past the top critical point moves the Fermi surface through a Lifshitz transition. At energy level E_2 , which is slightly below the pair of Weyl nodes, we observe that the initial Fermi surface splits into two. Generally, at energies between the two Lifshitz transition points, each projected Weyl node is enclosed by its own Fermi surface and therefore, each individual surface is topologically non-trivial, as shown in middle panel of Fig. 3b. The yellow arrows in Fig. 3b indicate the direction of Berry flux emanating from each projected Weyl node and non-trivial Fermi surface. As the energy level is further lowered, the Fermi surface undergoes a second Lifshitz transition. At energy level E_1 , which is similar to E_3 , a single Fermi surface again encloses both projected oppositely chiral charged Weyl nodes, and is therefore topologically trivial, as shown in the rightmost panel of Fig. 3b.

Performing a similar evaluation on the model Kramers Weyl metal in SG-16, the Fermi surface evolution is drastically different. The electronic band structure for the tight-binding

model of SG-16 is shown in Fig. 3c. Starting at E_1 , we observe two concentric Fermi surfaces around the projected Kramers Weyl nodes at the BZ center. Unlike the Fermi surface of a band-inversion Weyl semimetal, we instead here observe two distinct, oppositely chiral charged Fermi surfaces enclosing the projected Kramers Weyl node at the zone center. As shown in Fig. 3c, the inner Fermi surface is formed by the upper cone of the Kramers Weyl node, while the outer Fermi surface is formed by the lower cone. As the energy level is increased to E_2 , the non-trivial outer Fermi surface expands towards the zone boundary. At E_3 , each Kramers Weyl node has its own individual non-trivial Fermi surface. The topological properties of these Kramers Weyl Fermi surfaces therefore differ strongly from those observed or predicted in previous band-inversion Weyl semimetals [12–33]. Furthermore, the energy window corresponding to the presence of topologically non-trivial Fermi surfaces in Kramers Weyl metals, mainly determined by the bandwidth in the spinless limit, can be in the energy range of multiple eV. This property makes experimental observation of topological surface physics in Kramers Weyl metals promisingly plausible.

VI. Weyl Fermi arcs in Kramers theorem-enforced Weyl metals:

The appearance of surface states in Kramers Weyl metals also differs significantly from in band-inversion Weyl semimetals. In this section, we show the distinct distribution of topological Fermi arcs in a Kramers Weyl metal, using our tight-binding model of SG-16. In Fig. 4a we show the distribution of Kramers Weyl nodes at the bulk TRIMs. To study the emerging Fermi arc surface states, we consider the projection of Kramers Weyl nodes onto the (110)-surface. In Fig. 4b we show that on this surface, each TRIM has a projected Kramers Weyl node with chiral charge ± 2 . Pictured in Fig. 4c, we first calculate the bulk and (110)-surface states for when the SOC strength t^s is smaller than lattice hopping strength t^1 . Examining in Fig. 4d a constant energy contour at $E = -0.5$ eV reveals that the majority of the projected Kramers Weyl nodes are covered by bulk pockets that consequently conceal their Fermi arc surface states. However, the projected Kramers Weyl nodes at \bar{X} and \bar{M} are not covered by the projected bulk pockets and, as shown in Fig. 4d, exhibit connecting Fermi arc surface states. To check if the surface states around \bar{M} are consistent with the expected chiral charge projection, we calculate the energy-dispersion around a closed path encircling \bar{M} , as displayed in Fig. 4e. We observe two chiral surface states dispersing along the same \mathbf{k} direction, confirming that the path defined in Fig. 4d encloses a projected Kramers Weyl

node of chiral charge +2.

To study the effect of adiabatically increasing SOC, we present in Fig. 4f the electronic band structure of our SG-16 tight-binding model for t^s much larger than t^1 . As discussed earlier, irrespective of SOC strength, the Kramers Weyl nodes remain permanently pinned at the TRIMs. We find that the increase of SOC extensively distorts the bulk bands, allowing for Fermi arcs to be observed over a wider section of the projected surface BZ. Although the Kramers Weyl nodes are fixed in momentum space, they are still free to move in energy when SOC is tuned. The resulting constant energy contour at $E = -0.5$ eV for the (110) surface is shown in Fig. 4g. Under high SOC conditions, the projections of Kramers Weyl nodes are no longer concealed by the projections of bulk pockets and the Fermi arc connectivity becomes easily resolvable. Proceeding as before, the energy-dispersion calculation around a path encircling \overline{M} reveals two co-propagating chiral modes, and again confirms that the enclosed projected Kramers Weyl node has a +2 chiral charge. In general, all of the TRIMs in symmorphic chiral crystals are guaranteed to host Kramers Weyl nodes, and therefore these systems may host a novel topological Weyl metallic phase with large and well-separated Fermi arcs.

VII. Material candidates for Kramers Weyl metals:

The experimental realization of Weyl materials is a crucial step in the verification and continued development of topological condensed matter physics. As band-inversion Weyl nodes are “accidentally” created at generic \mathbf{k} points and therefore strongly depend on various material parameters, their theoretical prediction and experimental observation thus far has been exceedingly difficult: only about a dozen band-inversion Weyl semimetal candidates have been predicted [12–33, 39–41], and an even smaller subset have been experimentally confirmed [5, 6, 8–11, 42–47]. Furthermore, due to the uncertainty inherent when band-inversion is weak, several experimentally confirmed band-inversion Weyl semimetals [42–46], are still subject to intense debate, such as the possible Weyl semimetal state in $\text{W}(\text{Mo})\text{Te}_2$ crystals [42–46]. In Kramers Weyl metals, however, there is no band-inversion ambiguity and, as Kramers Weyl nodes are a guaranteed universal feature of chiral crystals, there are potentially thousands of new materials candidates.

Here we present three material candidates whose TRIMs host Kramers Weyl nodes: Ag_3BO_3 (SG-156), TiTe_2O_6 (SG-150), and Ag_2Se (SG-19). The former two are symmorphic

chiral crystals, while the latter is in a nonsymmorphic space group. The bulk BZ and TRIM points of Ag_3BO_3 are displayed in Fig. 5a. The electronic band structure of Ag_3BO_3 in the absence and presence of SOC is shown in Figs. 5b,c, respectively. As expected, for generic \mathbf{k} values the inclusion of SOC splits each band into two, except at the TRIMs because of Kramers theorem. For each TRIM, the isolated twofold-degenerate point is shown encircled in orange. Zooming in on the twofold-degenerate points at L and F , shown in the top and bottom panels of Fig. 5d, we observe Kramers Weyl nodes. We find that in fact *all* TRIMs in Ag_3BO_3 have isolated twofold-degenerate points that are linearly dispersing along all momentum-space directions. As shown earlier and consistent with our prediction for symmorphic chiral crystals, this indicates that all Kramers pairs at all TRIMs in Ag_3BO_3 are Kramers Weyl node.

Furthermore, we find two types of Fermi surfaces at the Fermi level: an electron pocket enclosing Γ and hole pockets enclosing L . Both electron and hole pockets are topologically non-trivial due to the enclosed chiral charge. The non-trivial topology of these Fermi surfaces could likely manifest itself in modified transport signatures, such as the chiral anomaly, in the presence of an external magnetic field.

Another material of interest is TlTe_2O_6 , whose bulk BZ and TRIM are shown in Fig. 5e. The electronic band structure along the high-symmetry lines, colored in blue in Fig. 5e, is displayed without and with SOC in Figs. 5f,g, respectively. As with Ag_3BO_3 in SG-156, a zoomed-in calculation near the Kramers points is shown in Fig. 5h, and reveals that Γ , A , H , and K are Kramers Weyl nodes. However, whereas Ag_3BO_3 is a metal, TlTe_2O_6 is a small-gap insulator with no Fermi surface at the Fermi level ($E = 0$). Thus, at the Fermi level none of the Kramers Weyl nodes have an effect on the low-energy physics. However, since the band gap in TlTe_2O_6 is small, a slight electron or hole doping could push the Fermi level to cut through the topologically non-trivial Fermi surfaces and, therefore, could provide a route towards experimentally accessing the properties of a Kramers Weyl metal.

Finally, we identify $\beta\text{-Ag}_2\text{Se}$ (SG-19), whose bulk BZ is shown in Fig. 5i, as a candidate nonsymmorphic Kramers Weyl material. The electronic band structure along the high-symmetry lines is displayed without and with SOC in Figs. 5j and k, respectively. In the absence of SOC, the low-energy electronic structure is dominated by a spin-degenerate pair of hole-like and electron-like bands around Γ , which meet in band-inversion nodes along $\Gamma\text{-X}$ and $\Gamma\text{-Y}$. SOC gaps out these nodes and at the same time induces a Kramers Weyl point

at Γ . The Fermi surface consists of two sheets with opposite Chern number enclosing the Γ point (and a very small trivial pocket along the Γ -X line).

Conclusion

In this work, we investigated a fundamental consequence of the combination of \mathcal{T} -symmetry and chirality in crystals with spin-orbit interactions. We found that in these systems, the TRIM points host Kramers theorem-enforced Weyl fermions. Though earlier efforts have characterized symmetry-enforced nodal physics in crystals [2, 37, 48, 49], the Kramers Weyl fermions introduced in this work represent the *smallest possible symmetry and geometry requirements* for nontrivial topological nodal physics, and therefore may enable access to potentially thousands of new, experimentally realizable systems with observable Fermi arcs.

To study the emergent properties of these crystal systems, we constructed a tight-binding model of a symmorphic chiral crystal in SG-16. We found that crystal structures in SG-16 possess Kramers theorem-enforced Weyl nodes and noted that, of the 65 chiral (Sohncke) space groups, crystals in the 26 symmorphic chiral space groups are *guaranteed to* possess Kramers Weyl nodes as universal features at *all* TRIM points. Crucially, we noted that Kramers Weyl nodes are not pairwise destructible, unlike band-inversion Weyl nodes [15–33]. Thus, if no \mathcal{T} -symmetry breaking perturbations are introduced and the symmetry of the underlying lattice is not increased through a structural transition, then, regardless of band-tuning conditions, the Kramers Weyl nodes remain fixed at each TRIM. Furthermore, because the partner of opposite chiral charge of any given Kramers Weyl node is at a neighboring TRIM, a Kramers Weyl metal is guaranteed to host the largest-possible momentum separation between Weyl nodes. In principle, this allows for the observation of large Fermi arc surface states when SOC is strong. Finally, we observed that for a large energy window, on the scale of multiple eV, the Fermi surface(s) can remain topologically non-trivial even if they do not enclose the projected Kramers Weyl nodes.

We additionally presented the symmorphic chiral crystals Ag_3BO_3 (SG-156) and TlTe_2O_6 (SG-150), and the nonsymmorphic chiral crystal Ag_2Se (SG-19), as materials candidates for realizing the Kramers theorem-enforced Weyl topological phase. The Kramers Weyl metal represents an entirely new class of globally symmetry-protected topological materials, which offers a promising platform for observing fundamental physics and manifesting new transport

properties with potential device applications.

Method

We performed first-principles calculations within the density functional theory (DFT) framework using the projector augmented wave method [50] as implemented in the VASP [51] package and the full-potential augmented plane-wave method as implemented in the package Wien2k [52]. The generalized gradient approximation (GGA) was used [53].

Acknowledgements

Work at Princeton was supported by the US Department of Energy under Basic Energy Sciences (Grant No. DOE/BES DE-FG-02-05ER46200). M.Z.H. acknowledges Visiting Scientist support from Lawrence Berkeley National Laboratory, and partial support from the Gordon and Betty Moore Foundation for theoretical work. H.L. is supported by the government of Singapore. B.J.W. acknowledges support through a Simons Investigator grant from the Simons Foundation to Charles L. Kane. F.S. acknowledges support from the Swiss National Science Foundation. The authors thank Professors Charles L. Kane and Randall Kamien from the University of Pennsylvania for helpful discussions on chirality.

[†] Electronic address: nilnish@gmail.com

[‡] Electronic address: mzhasan@princeton.edu

- [1] Flack, H. D., Chiral and Achiral Crystal Structure. *Helvetica Chimica Acta*, Vol. 86 (2003).
- [2] Mañes, J. L., Existence of bulk chiral fermions and crystal symmetry, *Phys. Rev. B* **85**, 155118 (2012)
- [3] Weyl, H., Elektron und gravitation. *I. Z. Phys.* **56**, 330-352 (1929).
- [4] Peskin, M.E., Schroeder, D. V., An introduction to Quantum Field Theory. Westview Press; First Edition edition (1995).
- [5] Xu, S.-Y., Belopolski, I., Alidoust, N., *et al.*, Discovery of a Weyl Fermion semimetal and topological Fermi arcs. *Science* **349**, 613-617 (2015).
- [6] Xu, S.-Y., Alidoust, N., Belopolski, I., *et al.*, Discovery of a Weyl fermion state with Fermi arcs in niobium arsenide. *Nature Physics* **11**, 748-754 (2015).

- [7] Lu, L., Wang, Z., Ye, D., *et al.*, Experimental observation of Weyl points. *Science* **349**, 622 (2015).
- [8] Lv, B. Q., Weng, B.B., Wang, X.P., *et al.*, Experimental discovery of Weyl semimetal TaAs. *Phys. Rev. X* **5**, 031013 (2015).
- [9] Xu, S.-Y., Belopolski, I., Sanchez, D. S., *et al.*, Experimental discovery of a topological Weyl semimetal state in TaP. *Science Advances*, Vol. **1** no.10, 1501902 (2015).
- [10] Belopolski, I., Xu, S.-Y., Sanchez, D. S., *et al.*, Criteria for directly detecting topological Fermi arcs in Weyl semimetals. *Phys. Rev. Lett.* **116**, 066802 (2016).
- [11] Xu, S.-Y., Belopolski, I., Sanchez, D. S., *et al.*, Spin polarization and texture of the Fermi arcs in the Weyl Fermion semimetal TaAs. *Phys. Rev. Lett.* **116**, 096801 (2016).
- [12] Hasan, M. Z., Kane, C. L., Topological Insulators. *Rev. Mod. Phys.* **82**, 3045-3067 (2010).
- [13] Qi, X.-L., Zhang, S.-C., Topological insulators and superconductors. *Rev. Mod. Phys.* **83**, 1057-1110 (2011).
- [14] Turner, A. M., Vishwanath, A., Beyond band insulators: topology of semi-metals and interacting phases. <http://arxiv.org/abs/1301.0330> (2013).
- [15] Murakami, S., Phase transition between the quantum spin Hall and insulator phases in 3D: emergence of a topological gapless phase. *New J. Phys.* **9**, 356 (2007).
- [16] Burkov, A. A. , Balents, L., Weyl Semimetal in a Topological Insulator Multilayer. *Phys. Rev. Lett.* **107**, 127205 (2011).
- [17] Balents, L., Weyl electrons kiss. *Physics* **4**, 36 (2011).
- [18] Xu, G., Weng, H., Wang, Z., *et al.*, Chern Semimetal and the Quantized Anomalous Hall Effect and HgCr₂Se₄. *Phys. Rev. Lett.* **107**, 186806 (2011).
- [19] Wan, X., Turner, A. M., Vishwanath, A. , Savrasov, S. Y., Topological semimetal and Fermi-arc surface states in the electronic structure of pyrochlore iridates. *Phys. Rev. B* **83**, 205101 (2011).
- [20] Ojanen, T., Helical Fermi arcs and surface states in time-reversal invariant Weyl semimetals. *Phys. Rev. B* **87**, 245112 (2013).
- [21] Huang, S.-M., Xu, S.-Y., Belopolski, I., *et al.*, A Weyl Fermion semimetal with surface Fermi arcs in the transition metal monpnictide TaAs class. *Nature Commun.* **6**, 7373 (2015).
- [22] Weng, H., Fang, C., Fang, Z., *et al.*, Weyl semimetal phase in non-centrosymmetric transition metal monophosphides. *Phys. Rev. X* **5**, 011029 (2015).

- [23] Lee, C-C., Xu, S-Y., Huang, S-M., *et al.*, Fermi surface interconnectivity and topology in Weyl fermion semimetals TaAs, TaP, NbAs, and NbP. *Phys. Rev. B* **92**, 235104 (2015).
- [24] Soluyanov, A. A., Gresch, D., Wang, Z., *et al.*, Type II Weyl Semimetals. *Nature* **527**, 495-498 (2015).
- [25] Sun, Y., Wu, S.-C., Ali, M.N., *et al.*, Prediction of the Weyl semimetal in the orthorhombic MoTe₂. *Phys. Rev. B* **92**, 161107 (2015).
- [26] Wang, Z., Gresch, D., Soluyanov, A.A., *et al.*, MoTe₂: A Type-II Topological Metal. *Phys. Rev. Lett.* **117**, 056805 (2016).
- [27] Chang, G., Xu, S.-Y., Sanchez, D.S., *et al.*, A strongly robust Weyl fermion semimetal state in Ta₃S₂. *Science Advances*, Vol. 2, No. 6, e1600295 (2016).
- [28] Chang, T.-R., Xu, S.-Y., Chang, G., *et al.*, Prediction of an arc-tunable Weyl Fermion metallic state in Mo_xW_{1-x}Te₂. *Nature Commun.* **7**,10639 (2016).
- [29] Wang, Z., Vergniory, M.G., Kushwaha, S., *et al.*, Time-Reversal Breaking Weyl Fermions in Magnetic Heuslers. arXiv: 1603:00479 (2016).
- [30] Chang, G., Xu, S.-Y., Zheng, H., *et al.*, Room-temperature magnetic topological semimetal state in half-metallic Heusler Co₂TiX (X=Si, Ge, or Sn). arXiv:1603.01255 (2016).
- [31] Chang, G., Singh, B., Xu, S.-Y., *et al.*, Theoretical prediction of magnetic and noncentrosymmetric Weyl fermion semimetal states in the R-Al-X family of compounds (R=rare earth, Al=aluminium, X=Si, Ge). arXiv:1604.02124 (2016).
- [32] Koepernik, K., *et al.*, TaIrTe₄ a ternary Type-II Weyl semi-metal. *Phys. Rev. B* **93**, 201101(R) (2016).
- [33] Autés, G., Troyer, M., Soluyanov, A. A., *et al.*, Robust Type-II Weyl Semimetal Phase in Transition Metal Diphosphides XP₂ (X = Mo, W). arXiv:1603.04624 (2016).
- [34] Watanabe, H., Po, H.C., Vishwanath, A., Zaletel, M.P., Filling constraints for spin-orbit coupled insulators in symmorphic and nonsymmorphic crystals. *Proc. Natl. Acad. Sci.* **112**, 14551 (2015).2
- [35] Wieder, B.J. and Kane, C.L., Spin-orbit semimetals in the layer groups. *Phys. Rev. B* **94**, 155108 (2016).
- [36] Nielsen, H. B., Ninomiya, M., The Adler-Bell-Jackiw anomaly and Weyl fermions in a crystal, *Physics Letters B*, **130**, 389-396 (1983).
- [37] Young, S. M., Zaheer, S., Teo, J.C.Y., *et al.*, Dirac Semimetal in Three Dimensions. *Phys. Rev.*

- Lett.* **108**, 140405 (2012).
- [38] Steinberb, J.A., Young, S.M., Zaheer, S., Kane, C.L., Bulk Dirac Points in Distorted Spinel. *Phys. Rev. Lett.* **112**, 036403 (2014).
 - [39] Wang, Z, Alexandradinata, A, Cava, R. J., *et al.*, Hourglass fermions. *Nature* **532**, (2016).
 - [40] Zhu, Z., Winkler, G. W., Wu, Q.-S., *et al.*, Triple Point Topological Metals. arXiv:1605.04653v2 (2016).
 - [41] Chang, G., Xu, S.-X., Huang, S-M., New fermions on the line in topological symmorphic metals. arXiv:1605.06831 (2016).
 - [42] Belopolski, I., Xu, S-Y., Ishida, Y., *et al.*, Unoccupied electronic structure and signatures of topological Fermi arcs in the type-II Weyl semimetal candidate $\text{Mo}_x\text{W}_{1-x}\text{Te}_2$. arXiv:1512.09099 (2015).
 - [43] Tamai, A., Wu, Q. S., Cucchi, I., *et al.*, Fermi Arcs and Their Topological Character in the Candidate Type-II Weyl Semimetal MoTe_2 . *Phys. Rev. X* **6**, 031021 (2016).
 - [44] Wu, Y., Mou, D., Jo, N. H., *et al.*, Observation of Fermi arcs in the type-II Weyl semimetal candidate WTe_2 . *Phys. Rev. B* **94**, 121113(R) (2016).
 - [45] Bruno, F. Y., Tamai, A., Wu, Q. S., *et al.*, Observation of large topologically trivial Fermi arcs in the candidate type-II Weyl semimetal WTe_2 . *Phys. Rev. B* **94**, 121112(R) (2016).
 - [46] Huang, L., McCormick, T. M., Ochi, M., *et al.*, Spectroscopic evidence for a type II Weyl semimetallic state in MoTe_2 . *Nature Materials* **4685**, doi:10.1038 (2016).
 - [47] Xu, S.-Y., Alidoust, N., Chang, G., *et al.*, Discovery of Lorentz-violating Weyl fermion semimetal state in LaAlGe materials. arXiv:1603.07318 (2016).
 - [48] Wieder, B.J., Kim, Y., Rappe, A.M., *et al.*, Double Dirac Semimetals in Three Dimensions. *Phys. Rev. Lett.* **116**, 186402 (2016).
 - [49] Bradlyn, B., Cano, J., Wang, Z., *et al.*, Beyond Dirac and Weyl fermions: Unconventional quasiparticles in conventional crystal. *Science* **353**, 5037 (2016).
 - [50] Kresse, G., Joubert, D., From ultrasoft pseudopotentials to the projector augmented-wave method. *Phys. Rev. B*, **59** 1758 (1999).
 - [51] Kresse G., Furthmüller J., Efficiency of ab-initio total energy calculations for metals and semiconductors using a plane-wave basis set. *Computational Materials Science*, **6**, 15 (1996).
 - [52] Blaha P., Schwarz K., Madsen G.K.H., *et al.*, An augmented plane wave plus local orbital program for calculating crystal properties. Vienna University of Technology, Vienna, Austria,

2001.

- [53] Perdew, J.P., Burke K., Ernzerhof M., Generalized gradient approximation made simple. *Phys. Rev. Lett.*, **77**, 3865 (1996).

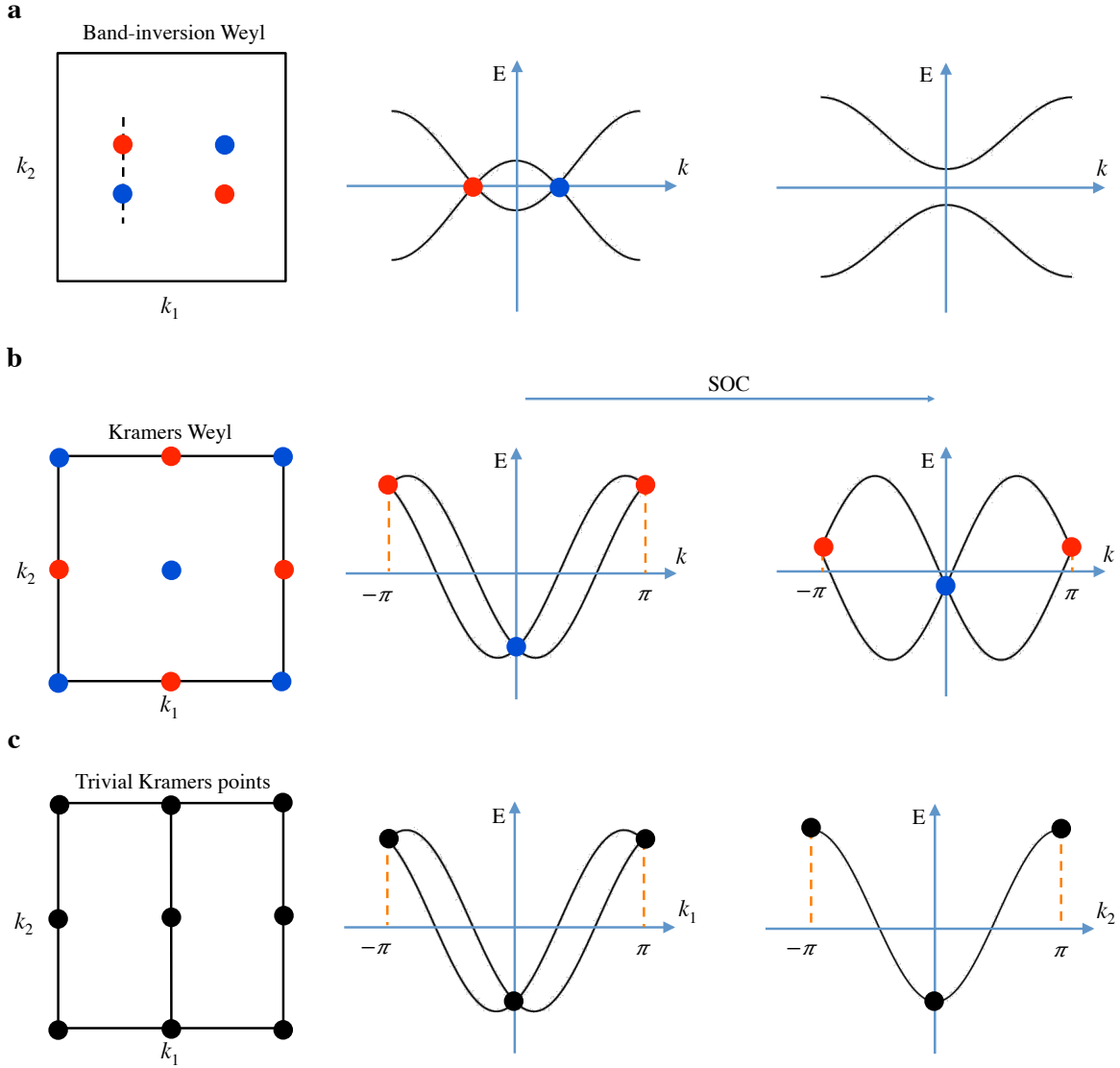


FIG. 1: **Kramers theorem-enforced Weyl nodes.** (a) Band-inversion generated Weyl nodes at generic points of the Brillouin Zone (BZ). The red and blue marks indicate Weyl nodes of opposite chiral charge. The energy-momentum separation of the band-inversion generated Weyl nodes is directly determined by the strength of the band-inversion (middle panel) and the nodes may be pairwise annihilated by pulling the conduction and valence band apart by increasing SOC (right-most panel). (b) In the presence of \mathcal{T} -symmetry, Kramers pairs form at the TRIMs. When the Kramers pairs are isolated twofold degenerate points with linear dispersion in all directions, they are, by definition, Weyl nodes. The creation of Kramers theorem-enforced Weyl nodes does not require band-inversion, and they are guaranteed to have a large separation in momentum space. As long as \mathcal{T} -symmetry is preserved, Kramers Weyl nodes remain pinned at the TRIMs and cannot

FIG. 1: be pairwise annihilated. (c) Kramers pairs are no longer Weyl nodes when they are not isolated in momentum space. The addition of extra symmetries, such as \mathcal{I} , roto-inversions, or nonsymmorphic symmetries, may generate extra degeneracies that connect Kramers points along some \mathbf{k} direction and can nullify some of the topological physics.

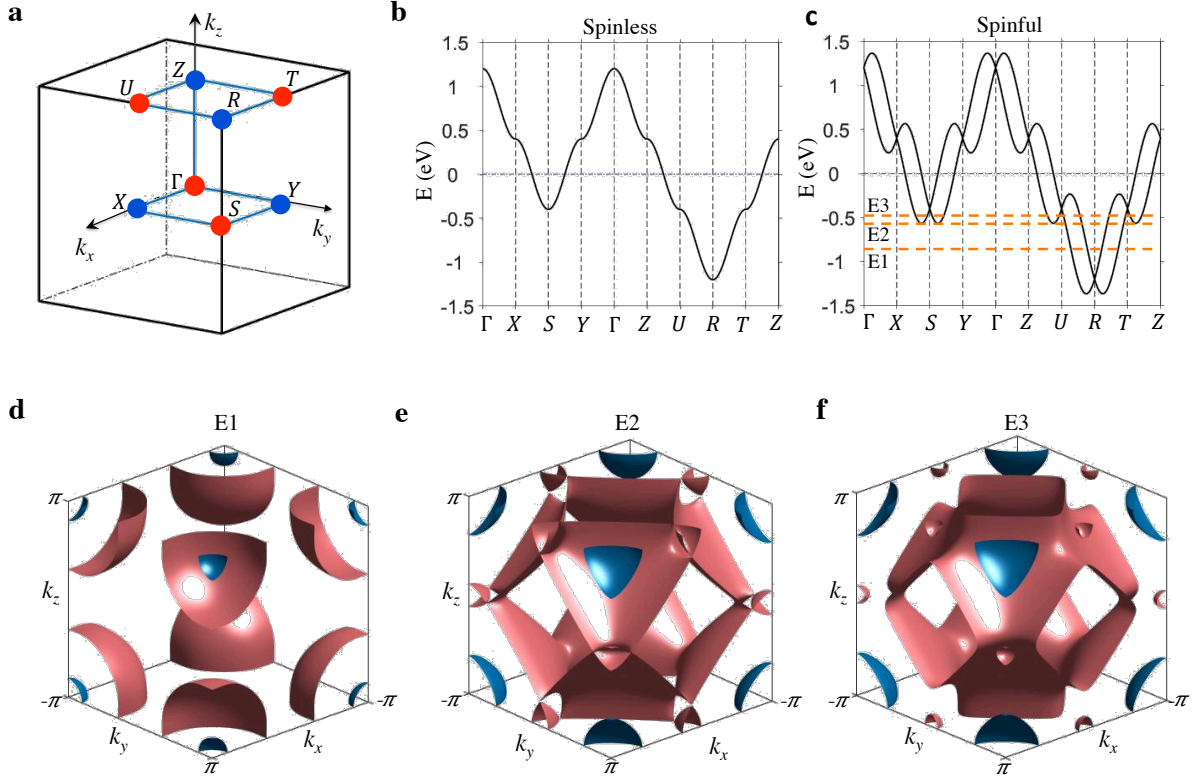


FIG. 2: Tight-binding model for a Kramers Weyl metal in Space Group 16 (SG-16).

(a) The distribution of chiral charge in the bulk BZ of a Kramers Weyl metal in SG-16. The red and blue colors indicate Kramers Weyl nodes of opposite chiral charge at the TRIMs in the presence of SOC. (b) The band structure for the SG-16 tight-binding model in the absence of SOC. Note that the Fermi level cuts through the middle of the band. (c) Turning on SOC results in the doubly-degenerate band in panel (b) splitting into two bands. These two bands are separated from each other for generic \mathbf{k} values, except at the TRIMs. At each TRIM, Kramers pairs are observed as isolated twofold-degenerate Weyl nodes. (d, e, f) The bulk Fermi surfaces for energy levels E1, E2, and E3, respectively. The color red corresponds to a positive Chern number and blue represents a negative Chern number. At energy level E1, there are two concentric spheres enclosing the R -points. As the energy level is tuned to E3, the Fermi surface with positive Chern number splits into two.

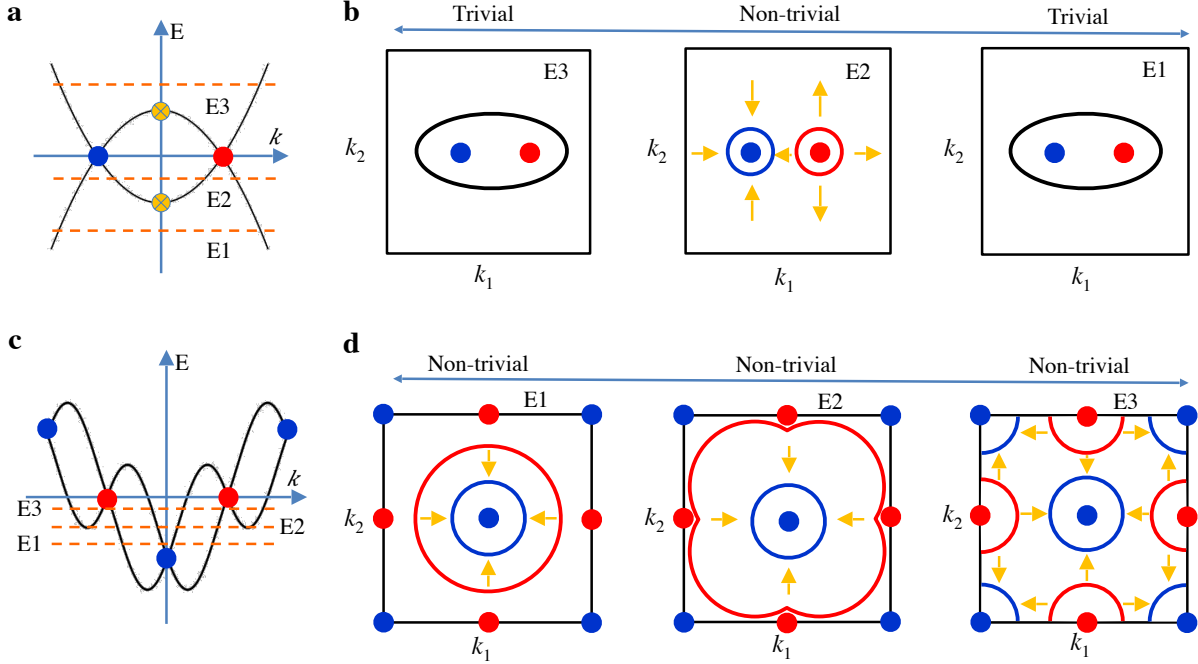


FIG. 3: Topological Fermi surface of Kramers Weyl nodes. (a) The electronic band structure of a conventional band-inversion Weyl semimetal. The blue and red colors represent Weyl nodes of opposite chiral charge. The yellow colors indicate the points where a Lifshitz transition occurs. (b) The sequence of Fermi surfaces shown are for energy levels E1, E2, and E3, which are annotated in panel (a). The red and blue coloring of the Fermi surfaces indicates a positive or negative Chern number, respectively. The net chiral charge enclosed by the black Fermi surface is zero and, therefore, it is topologically trivial. The yellow arrows illustrate the flow of Berry curvature from each topologically non-trivial Fermi surface. The Fermi surface of a band-inversion Weyl semimetal is topologically non-trivial for the energy window defined by the degree of band-inversion, which is typically small. (c) The electronic band structure of a Kramers Weyl metal. (d) The Fermi surface for energy levels E1, E2, and E3, annotated in panel (c). The Fermi surface of a Kramers Weyl metal remains topologically non-trivial from the bottom to the top of the bands. Thus, the energy window corresponding to a topologically non-trivial Fermi surface for a Kramers Weyl metal can be as large as multiple eV.

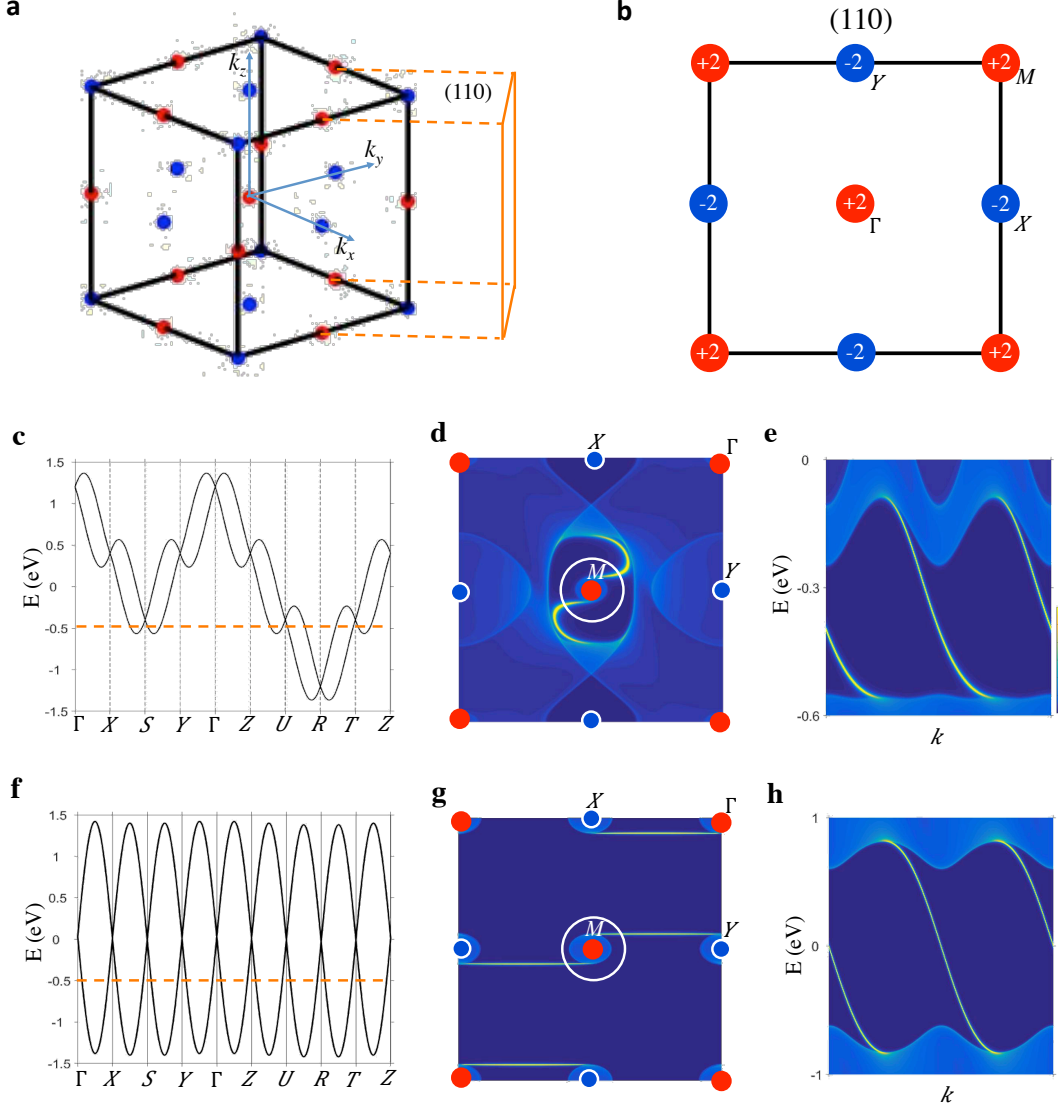


FIG. 4: **Fermi arc surface states in a Kramers Weyl metal.** (a) The chiral charge distribution of Kramers Weyl nodes in the bulk BZ of SG-16. The (110) surface is shown in orange with added dashed lines indicating the projection of Kramers Weyl nodes. (b) The projected chiral charge on the (110) surface. The number labeled in each red and blue marking represents the projected chiral charge at that point. (c) The electronic band structure of a Kramers Weyl metal in SG-16 from the tight-binding model presented in this paper, set with t_s smaller or of the same order as t_l (d) The surface states of the (110) surface at -0.5 eV. Indicated in panel (c) by the orange-dashed line is the energy-level corresponding to (d). (e) Energy-dispersion calculation of surface states along the path defined by the white circles enclosing the \bar{M} -point. The number of chiral surface states is consistent with the projected chiral charge. (f) We adiabatically change the electronic band

FIG. 4: structure of the Kramers Weyl metal by increasing the SOC interaction term t_s relative to the lattice hopping term t_l . Panel (f) shows the band structure when t_s is much larger than t_l . (g, h) The surface states calculations from the bands in panel (f) at -0.5 eV.

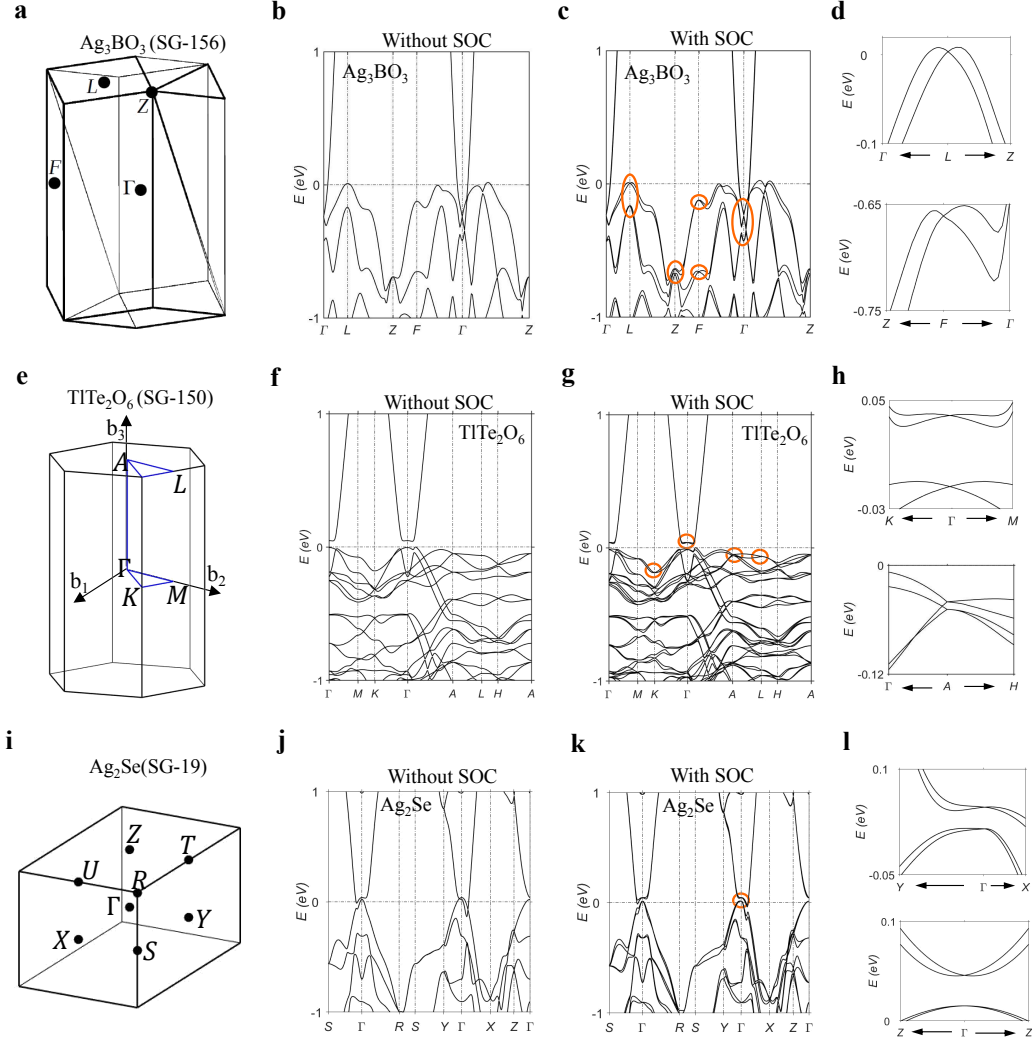


FIG. 5: **Electronic band structures of Ag_3BO_3 , TiTe_2O_6 , and Ag_2Se .** (a,) The bulk Brillouin zone (BZ) of Ag_3BO_3 in space group 156 with Kramers points at Γ , F , L and Z labeled. (b, c) The band structure of Ag_3BO_3 in the absence and presence of spin-orbit coupling (SOC), respectively. All of the Kramers points of Ag_3BO_3 are isolated Weyl nodes after the inclusion of SOC, and are shown enclosed by orange circles. (d) Zooming into the bands in the vicinity of F and L , we observe isolated twofold-degenerate points with linear dispersion, confirming that they are Kramers Weyl nodes. (e) Bulk BZ of TiTe_2O_6 in space group 150 with Kramers points at Γ , M , A , L labeled. (f, g) The band structures of TiTe_2O_6 in the absence and presence of SOC, respectively. All of the Kramers points in TiTe_2O_6 are Weyl nodes after the inclusion of SOC, and are shown enclosed by orange circles in (g). (h). The zoomed-in view of the bands in the vicinity of Γ and A . (i) Bulk BZ of Ag_2Se in space group 19 with TRIM points labeled. (j, k) The band structures of Ag_2Se in the absence and presence of SOC, respectively. The Kramers points on Γ

FIG. 5: in Ag_2Se are Kramers Weyl nodes after the inclusion of SOC, which are shown enclosed by orange circles in (k). (1) The zoomed-in view of the bands in the vicinity of Γ .